RSC Advances

PAPER

View Article Online
View Journal | View Issue

Cite this: *RSC Adv.*, 2023, **13**, 22070

A new strategy to exploit maximum rate performance for aqueous batteries through a judicious selection of MOF-type electrodes†

Kosuke Nakamoto, *[a] Junwen Bai,[b] Minyan Zhao,[b] Ryo Sakamoto, [a] Liwei Zhao,[a] Masato Ito, *[a] Shigeto Okada, *[a] Eiji Yamamoto, [c] Haruno Murayama [c] and Makoto Tokunaga [c]

A metal–organic framework (MOF) having a redox active 1,4,5,8-naphthalenetetracarboxdiimide (NDI) derivative in its organic linker shows excellent rate performance as an electrode material for aqueous batteries thanks to its large pores. Among aqueous electrolytes examined, K^+-based ones exhibit the highest rate performance, which is caused by the highest mobility of the smallest hydrated K^+ ion not only in the aqueous electrolyte but also in the electrode. Since the use of a counter electrode with insufficiently small pores for the full-cell configuration offsets this merit, our study may lead to a conclusion that the maximum rate performance for aqueous batteries will be accomplished only through further elaboration of both electrode materials with sufficiently large pores, in which hydrated ions can travel equally fast as those in the electrolyte.

Received 13th May 2023
Accepted 13th July 2023

DOI: 10.1039/d3ra03187j

rsc.li/rsc-advances

Introduction

With the increasing demand for large-scale energy storage to meet the huge energy consumption, aqueous batteries have gained much attention as post lithium-ion batteries due to their attractive features such as safety, low cost, and high power.[1–3] Recently, alkaline metal (Li, Na, K) ion batteries with non-conventional aqueous electrolytes showing electrochemical window beyond the theoretical value (1.23 V) have provided renewed opportunities for various active electrode materials.[4] In contrast with inorganic electrode active materials, the redox active organic counterparts[5–10] have a higher degree of flexibility in materials design and their molecular modification may not only finely tune their redox potential but also add properties that affect intermolecular forces to change their solubility, surface area (porosity), and so on. 1,4,5,8-naphthalenetetracarboxdiimide derivatives (NDIs), which are readily prepared by dehydrative condensation of naphthalene-1,4,5,8-tetracarboxylic dianhydride (NDA) with a variety of primary amines, have been one of the most promising organic anode materials for aqueous batteries.[11–13] As illustrated in Scheme 1, the pair of two carbonyl groups either at 1 and 5 or at 4 and 8 positions undergo a reversible two electron redox reaction with concomitant change of resonance form in the naphthalene core. The parent 1,4,5,8-naphthalenetetracarboxdiimide (H_2NDI) was an exceptionally poor anode material, possibly because its NH groups are susceptible to irreversible reduction to generate a dianion, which is not hydrophobic enough to persist in the electrode but dissolves into aqueous electrolyte prior to the reversible redox reaction.[14] In contrast, a polymeric NDI derived from hydrazine was successfully employed as a durable anode for aqueous batteries.[15,16] Unfortunately, however, its rate performance was only modest considering high ionic conductivity of aqueous electrolyte, which suggested that non-uniform surface of polymeric material could hinder smooth insertion of guest cation from aqueous electrolyte.[17] In order to overcome above-mentioned shortcoming and to exploit reliable redox behaviors of NDIs, we focused on NDI-based metal–organic frameworks (MOFs)[18] as active materials which enable the smooth insertion of guest cation. To the best of our knowledge, there have been no reports for rocking chair-type

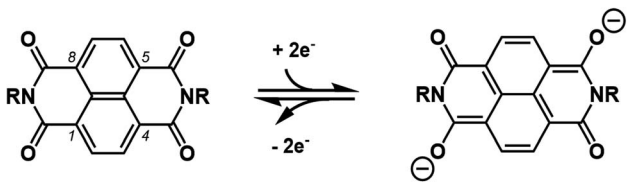

Scheme 1 Two electron reduction/oxidation reaction of NDIs.

[a]*Institute for Materials Chemistry and Engineering, Kyushu University, 6-1 Kasuga-koen, Kasuga, Fukuoka, 816-8580, Japan. E-mail: nakamoto@cm.kyushu-u.ac.jp; mito@cm.kyushu-u.ac.jp; okada.shigeto.893@m.kyushu-u.ac.jp*

[b]*Interdisciplinary Graduate School of Engineering Sciences, Kyushu University, 6-1 Kasuga-koen, Kasuga, Fukuoka, 816-8580, Japan*

[c]*Department of Chemistry, Graduate School of Science, Kyushu University, 744 Motooka, Nishi-ku, Fukuoka, 819-0395, Japan*

† Electronic supplementary information (ESI) available. See DOI: https://doi.org/10.1039/d3ra03187j

monovalent cation-conducting aqueous batteries using such MOFs, though Prussian-blue analogues (PBAs) may have been applied as conventional MOF-type electrodes.[19] These situations may be caused mainly by the three reasons; (i) the MOF-type electrodes should have adequate water resistance, (ii) their redox potentials should locate within the stability window of aqueous electrolyte, (iii) they should not have unnecessarily large molecular weights because their redox-silent parts inevitably attenuate their theoretical capacity. On the other hand, Dincă and co-workers recently developed $[Zn(dmpz)_2NDI]_n$-MOF, which undergoes a two-electron reaction of NDI in aqueous electrolyte to serve as electrochromic materials.[20,21] It has NDI units functionalized with two 3,5-dimethylpyrazole (dmpzH) ligands, which generate infinite [metal(μ-pyrazolate)$_2$]$_n$ chains with tetrahedral Zn(II) in the orthogonal direction.[22] Thus formed staggered parallelogram having $(dmpz)_2NDI$ molecule on each side provides a wide channel whose surface should be easily accessible by aqueous electrolyte. Most importantly, $[Zn(\mu\text{-}dmpz)_2]_n$ chains should be stable toward a range of aqueous solutions unless they are too acidic or basic.[23–26] Therefore, we envisaged that $[Zn(dmpz)_2NDI]_n$-MOF should serve as a durable anode material in the aqueous battery, and it could show greater rate and cycle performances than conventional NDI-based anode materials.

We have been engaged in the development of aqueous battery using PBAs as active material with non-conventional aqueous electrolytes.[27,28] In these studies, we became interested in the generally accepted idea that K^+ ion is less Lewis acidic compared with Li^+ or Na^+ ions, and its aqueous solutions display the lowest viscosity, and therefore K^+-based aqueous electrolytes have an advantage in terms of rate performance.[29–36] Significantly, however, this hypothesis may not be applicable unless these charge carriers may behave similarly within the electrode to those in the electrolyte. In fact, Cui and co-workers claimed[37] that K^+-based aqueous electrolytes have no kinetic advantage in the particular case of PBA electrodes.[38–45] Their result suggested that the pore size around 5 Å provided by the cyano-bridged MOF structure of PBAs (Fig. 1) may restrict the mobility of K^+ ions as compared to the aqueous solution state, thereby cancelling out its kinetic merit. On the other hand, the pore size around 16 Å provided by $[Zn(dmpz)_2NDI]_n$-MOF (Fig. 1) is large enough to allow accommodation of K^+ ions in the similar environment to that in the aqueous solution, and has a greater chance of maximizing the rate performance of K^+-based aqueous electrolytes. Therefore, we began our study by electrochemical characterization of $[Zn(dmpz)_2NDI]_n$-MOF as an anode material, initially in 17 m $NaClO_4$ aqueous electrolyte to confirm the benefit provided by its open-framework structure. Next, aqueous electrolytes with several cations having identical anion and constant concentration (8 m AOTf, A = Li, Na, K, trifluoromethanesulfonate salts) were used with this anode to assess the rate performance of these cations. As a result, we obtained conclusive evidence that K^+-based aqueous electrolytes may offer a non-negligible kinetic advantage, if they are combined with electrodes with large pore size and readily accessible uniform surface. Herein we describe these results.

Results and discussion

Viability of MOF-type electrode

Our initial study focused on the electrochemical characterization of $[Zn(dmpz)_2NDI]_n$-MOF as an anode material in aqueous battery. $[Zn(dmpz)_2NDI]_n$-MOF was prepared according to the reported method,[20] and its disc-shaped electrode composite was fabricated by mixing it with conductive carbon and binder to measure its electrochemical properties in 17 mol kg^{-1} (m) $NaClO_4$ aqueous electrolyte.[27,28,46–48] Control experiments were performed with H_2NDI and $H_2(dmpz)_2NDI$, which lacks infinite [metal(μ-pyrazolate)$_2$]$_n$ chains but still carries dmpzH end groups capable of intermolecular H-bonding, under otherwise identical conditions. These results are listed in Fig. 2b–d along with the schematic images of molecular and crystal structures for H_2NDI, $H_2(dmpz)_2NDI$, and $[Zn(dmpz)_2NDI]_n$-MOF (Fig. 2a). The theoretical capacity for $2e^-$ redox reaction (Table 1) for H_2NDI, $H_2(dmpz)_2NDI$, and $[Zn(dmpz)_2NDI]_n$-MOF calculated by their molecular weights is 202, 118, 80 mA h g^{-1}, respectively, and their initial practical reversible capacity proved to be approximately equal as shown in the Fig. 2b. These results indicated that the electrochemical behavior for the three materials commonly originates from the redox reaction of their

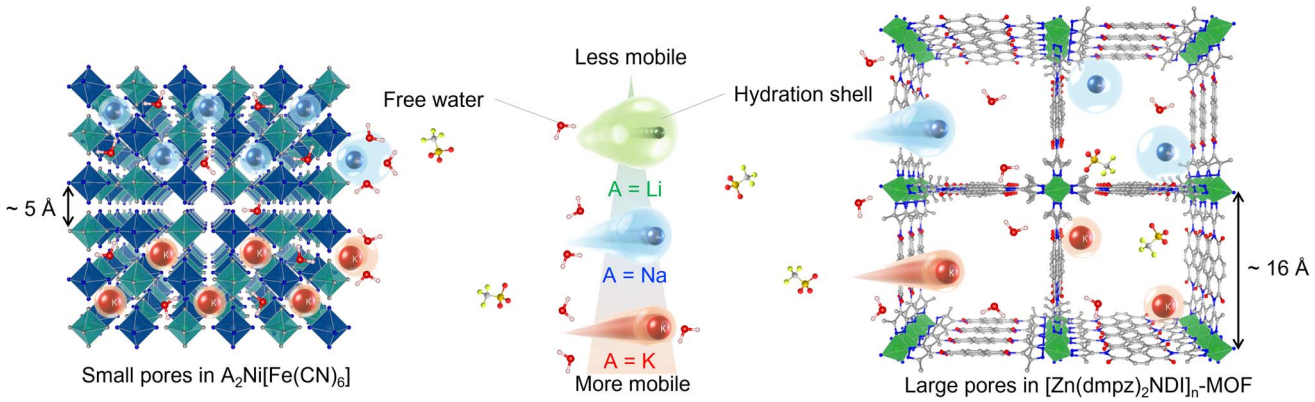

Fig. 1 Schematic images for illustration of relative size of hydrated ions, triflate anions, water molecules towards pores of electrode materials.

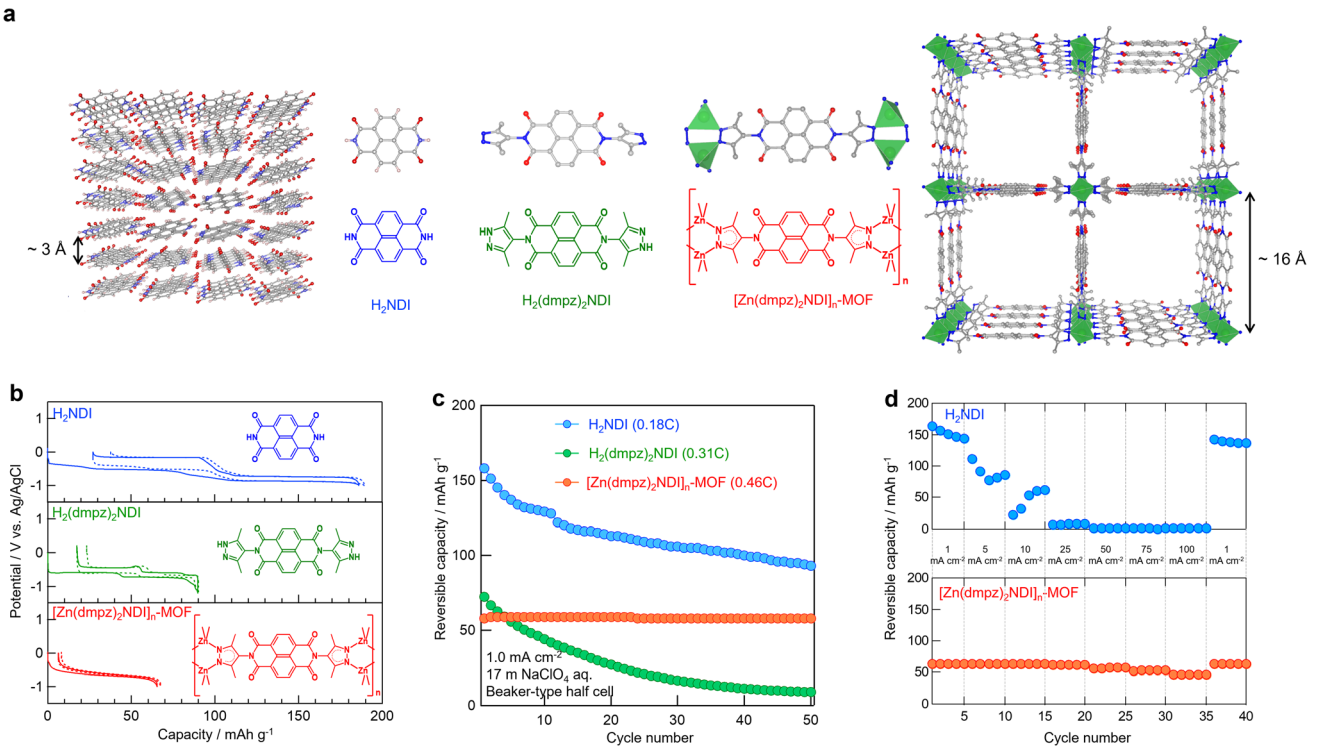

Fig. 2 (a) Schematic images of crystal and molecule structures. (b) 1st and 2nd discharge/charge profiles and (c) the cyclability of half cell in 17 m $NaClO_4$ aq electrolyte, for H_2NDI (blue), $H_2(dmpz)_2NDI$ (green), and $[Zn(dmpz)_2NDI]_n$-MOF (red), respectively. (d) Rate performance of H_2NDI (upper) and $[Zn(dmpz)_2NDI]_n$-MOF (lower) of half cell in 17 m $NaClO_4$ aq electrolyte.

Table 1 Molecular weight and theoretical capacity of active materials

	MW/g mol^{-1}	$2e^-$ theoretical capacity/mA h g^{-1}
H_2NDI	266	202
$H_2(dmpz)_2NDI$	454	118
$[Zn(dmpz)_2NDI]_n$-MOF·2DMF	666	80

NDI moiety and that the $[Zn(dmpz)_2]_n$ chains in $[Zn(dmpz)_2NDI]_n$-MOF may remain unchanged in 17 m $NaClO_4$ aqueous electrolyte. Also of note is that the overpotential within the initial discharge/charge cycles proved to be the smallest for $[Zn(dmpz)_2NDI]_n$-MOF and increased in the order of $[Zn(dmpz)_2NDI]_n$-MOF, $H_2(dmpz)_2NDI$, and H_2NDI. We believe that these results reflect how easily the charge carrier Na^+ ion (guest) can insert into and extract from the three NDIs (host). As shown in Fig. 2a, $[Zn(dmpz)_2NDI]_n$-MOF has a porous structure to easily accommodate the guests from all directions. In contrast, H_2NDI stacks in a dense manner because of its flat molecular structure and, therefore, the accommodation of the guests should require some structural change in the solid state. $H_2(dmpz)_2NDI$ may form a less dense solid-state structure compared with H_2NDI, since its dmpzH groups are non-coplanar to the NDI group and its molecular structure is no longer as flat as H_2NDI. Nevertheless, $H_2(dmpz)_2NDI$ could not accommodate the guests as easily as $[Zn(dmpz)_2NDI]_n$-MOF. These speculations may be consistent with the cyclability shown in Fig. 2c. The reversible capacity for H_2NDI as well as $H_2(dmpz)_2NDI$ gradually decreased from the initial values (158 and 72 mA h g^{-1}, and 78% and 61% compared with their theoretical capacities respectively) along with repeated cycles, while the reversible capacity for $[Zn(dmpz)_2NDI]_n$-MOF never attenuated throughout examined cycles (58 mA h g^{-1} for 1–50 cycles, 73% of capacity utilization compared with it theoretical capacity). Therefore, the repeated insertion and extraction of Na^+ ion into and out of these materials should deteriorate the pristine solid-state structures of H_2NDI and $H_2(dmpz)_2NDI$ having only weak intermolecular forces but should not affect the original porous structure of $[Zn(dmpz)_2NDI]_n$-MOF thanks to its robust $[Zn(dmpz)_2]_n$ framework. Fig. 2d illustrates the rate performance for H_2NDI and $[Zn(dmpz)_2NDI]_n$-MOF at different current densities. While the reversible capacity for H_2NDI decreased with increasing current density and it became unobservable above 25 mA cm^{-2} (12C), $[Zn(dmpz)_2NDI]_n$-MOF showed almost constant reversible capacity around 60 mA h g^{-1} within the range of 1–100 mA cm^{-2} (0.46–46C). These results clearly suggested that the porous and robust structure of electrode materials should be beneficial for high-rate and long-life battery.

Redox and Na^+-ion storage mechanisms of $[Zn(dmpz)_2NDI]_n$-MOF

To gain deeper insight on the electrochemical behavior of $[Zn(dmpz)_2NDI]_n$-MOF in 17 m $NaClO_4$ aqueous electrolyte along with possible structural change (Fig. 3a), the disc pellets

were disassembled from the electrochemical cell either after the first discharge or the first charge (Fig. 3b) to compare these used electrodes with the unused one by FT-IR (Fig. 3c), XPS (Fig. 3d), and XRD (Fig. 3e). In this *ex situ* FT-IR study, the unused sample (i) showed two C=O stretching peaks at 1681 and 1720 cm^{-1}, while the new shoulder peak at 1665 cm^{-1} appeared in the discharged sample (ii) and it disappeared in the charged sample (iii). This new peak may be assignable to the elongated C–O bonds[13] in the reduced form of the NDI group depicted in Scheme 1. Similar change during the discharge/charge sequence was also observed in *ex situ* XPS (Fig. 3d). Only in the case of the sample (ii), noticeable new signals appeared at 286 eV for C1s and 532 eV for O1s, respectively. These signals were not observed in the samples (i) or (iii), both of which displayed signals at 288 eV for C1s and 535 eV for O1s, respectively. We believe that the new signals are typical for C–O^- structure and the original signals are for C=O structure, though overlaps by the signal of inseparable conductive carbon made these interpretation inconclusive.[49] Furthermore, *ex situ* XRD showed shift in peaks towards lower angles along with discharge from (i) to (ii), whereas that towards higher angles with charge from (ii) to (iii). These results may represent the reversible accommodation of Na^+ ion into $[Zn(dmpz)_2NDI]_n$-MOF from 17 m $NaClO_4$ aqueous electrolyte with concurrent redox reaction of the NDI moiety.

Encouraged by the stable electrochemical performance of $[Zn(dmpz)_2NDI]_n$-MOF in 17 m $NaClO_4$ aqueous electrolyte, we next assembled a Na-ion battery comprised of $[Zn(dmpz)_2NDI]_n$-MOF and $Na_2Ni[Fe(CN)_6]$ PBA as electrodes and 17 m $NaClO_4$ as aqueous electrolyte. As shown in Fig. 3g, this rocking chair-type aqueous battery displayed cell voltage of *ca.* 1 V, which was in good agreement with cyclic voltammogram of separate electrodes shown in Fig. 3f; −0.5 V for $[Zn(dmpz)_2NDI]_n$-MOF and +0.5 V for $Na_2Ni[Fe(CN)_6]$ PBA (*vs.* Ag/AgCl) in 17 m $NaClO_4$ aqueous electrolyte. Notably, this battery showed virtually no capacity decay over 10 000 cycles (Fig. 3h).

Better compatibility of hydrated K^+-ion electrolyte with $[Zn(dmpz)_2NDI]_n$-MOF

To identify which alkaline ion would perfectly suit the present battery of $[Zn(dmpz)_2NDI]_n$-MOF anode and $Na_2Ni[Fe(CN)_6]$ PBA cathode, we next turned our attention on aqueous electrolytes having alkaline triflates (SO_3CF_3) because they show commonly high solubility in water irrespective of alkaline ion, which is a marked contrast to those having alkaline ClO_4 (Table 2). We first studied pH (◆) and ionic conductivity (●) of aqueous AOTf solutions (A = Li, Na, K) at varying concentration (Fig. 4a). The pH of AOTf solution ranked in the order of K^+ > Na^+ > Li^+ at the same concentration, but their individual values

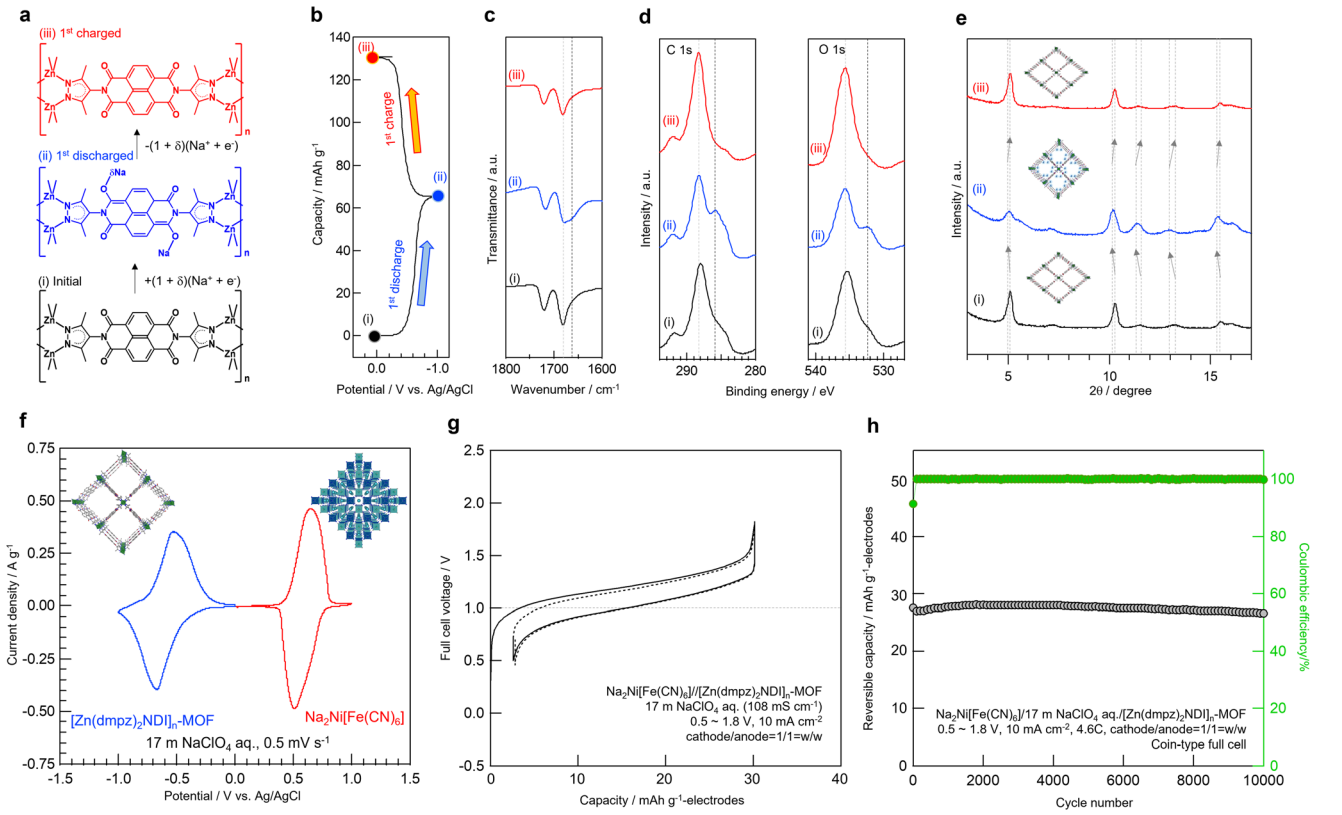

Fig. 3 (a) Possible structural change of $[Zn(dmpz)_2NDI]_n$-MOF upon electrochemical reaction in 17 m $NaClO_4$ aq. (b) Origin of the samples; (i) unused sample, (ii) used sample after discharging down to −1.0 V, and (iii) used sample after charging up to 0.0 V *vs.* Ag/AgCl. (c) *Ex situ* FT-IR. (d) *Ex situ* XPS. (e) *Ex situ* XRD. (f) Cyclic voltammetry of $[Zn(dmpz)_2NDI]_n$-MOF anode (blue) and $Na_2Ni[Fe(CN)_6]$ cathode (red) in 17 m $NaClO_4$ aq along with the schematic image of their initial structures. (g) 1st and 2nd charge/discharge profiles for the full-cell of $Na_2Ni[Fe(CN)_6]$//$[Zn(dmpz)_2NDI]_n$-MOF in 17 m $NaClO_4$ aq electrolyte. (h) Cyclability for the full-cell.

Table 2 Saturated concentration of alkaline salts with different anions in water

Concentration/mol kg^{-1}	Li^+	Na^+	K^+
F^-	0.05	1	18
$SO_3CF_3^-$	21	9	19
$N(SO_2CF_3)_2^-$	21	9	1
ClO_4^-	6	17	0.1

linearly decreased along with the increasing concentration. These results were not surprising because the Lewis acidity of the solute may give a proportional effect on the Brønsted acidity of its aqueous solution. The ionic conductivity (●) also ranked in the order of K^+ > Na^+ > Li^+ at the same concentration. However, their individual values became maximum at different concentrations around 5–7 m and decreased either at lower or higher concentrations. Since all AOTf solutions showed acceptably good ionic conductivity at the concentration of 8 m (molar ratio of solute and water is *ca.* 1 : 7), we next studied the structure of these particular AOTf solutions by FT-IR and roughly estimated their electrochemical stability window by linear sweep voltammetry (LSV). Fig. 4b focuses on the broad peaks centered at 3462, 3442, and 3432 cm^{-1}, which were observed in the FT-IR measurement for 8 m LiOTf, NaOTf, and KOTf solutions, respectively. It has been well documented that the O–H stretching in water is blue shifted upon destruction of its ice-like structure, which is caused by the hydration of Lewis acidic metal ion.[35,36,46,47,50] Predictably, the more Lewis acidic Li^+ ion should bind a greater number of Lewis basic water molecules to form a larger hydrated ion in 8 m LiOTf solution, whereas the less Lewis acidic K^+ ion may form a smaller hydrated ion in 8 m KOTf solution. The highlighted areas in Fig. 4c denote the electrochemical stability windows, which

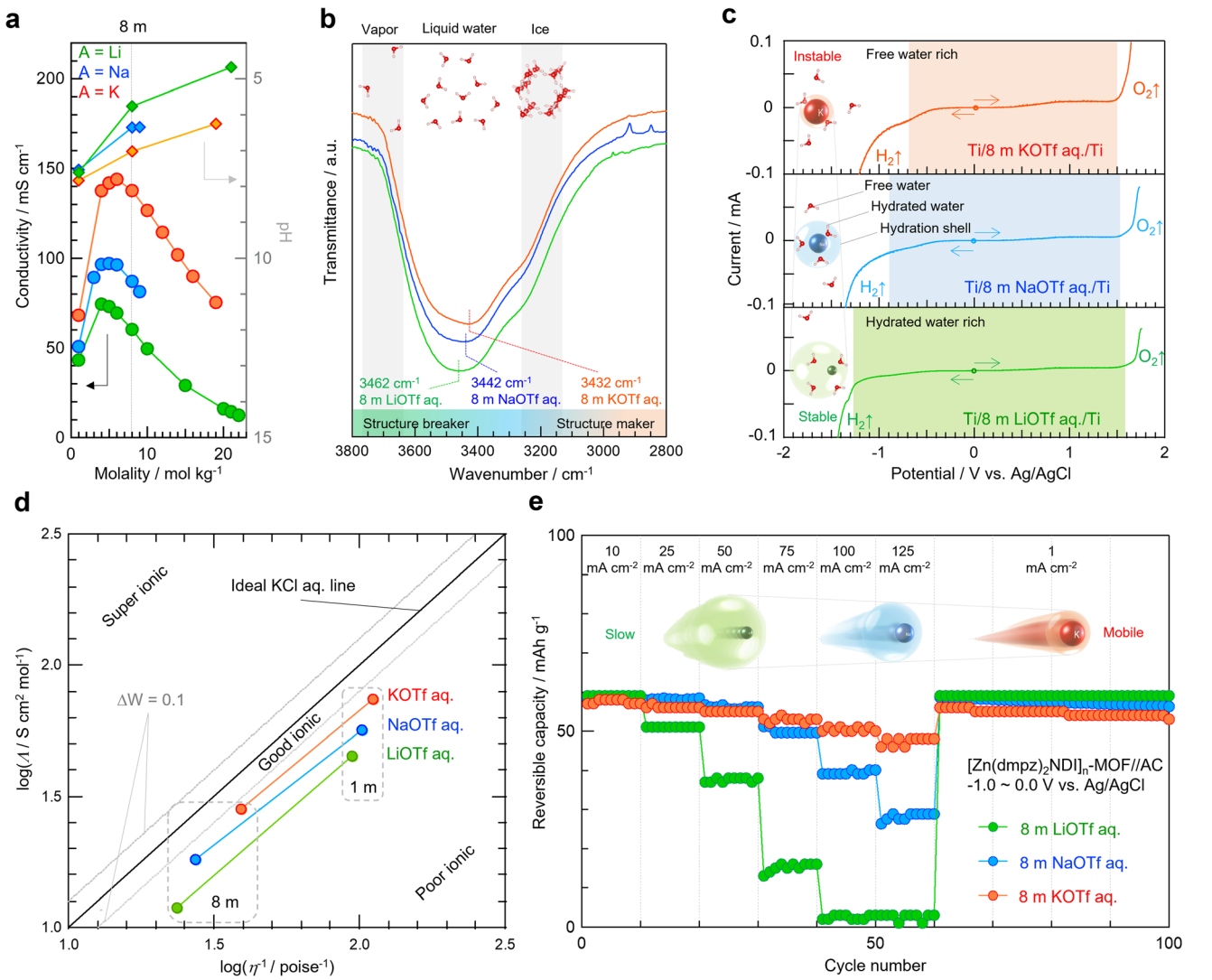

Fig. 4 (a) pH and ionic conductivity of AOTf aq. (b) FT-IR spectra. (c) LSVs on Ti current collector of 8 m AOTf aq (the hatch sections show estimated potential windows). (d) Walden plot of 1 m and 8 m AOTf aq. (e) Rate performance of $[Zn(dmpz)_2NDI]_n$-MOF in 8 m AOTf aq (A = Li, Na, K).

were derived from oxidation/reduction waves obtained by LSV measurements using titanium mesh. The window became wider in the order of $K^+ < Na^+ < Li^+$, which may be reasonable if Lewis acidic metal ion decreases the number of free water molecules, which are more readily subjected to electrolysis than coordinated water molecules. Also noteworthy is that the three potentials for the oxidation of 8 m AOTf solutions were almost identical, while those for the reduction varied significantly. This may be attributable to the different solubility of passivation layers on the electrode, whose large part should be composed of alkaline fluorides that are generated upon the reductive decomposition of OTf.[51–53] Specifically, sparingly soluble LiF can form a robust passivation layer which can lower the reduction boundary effectively, whereas readily soluble KF cannot play a similar role.

Fig. 4d summarizes the Walden plot[54] for the three AOTf solutions at the concentration of 1 m as well as 8 m. These data were collected by the calculation using parameters listed in Table 3. Under both diluted and concentrated conditions, all data were close to "good ionic" area and KOTf solutions were slightly better ionic and less viscous than NaOTf or LiOTf. Fig. 4e illustrates the rate performance for the half-cell of $[Zn(dmpz)_2NDI]_n$-MOF electrode in 8 m AOTf aqueous electrolytes at different C-rates. The difference of reversible capacity between three electrolytes became apparent when the current density was gradually increased. The initial reversible capacity at 10 mA cm^{-2} (4.6C) was almost halved or lost at 125 mA cm^{-2} (58C) in the case of NaOTf or LiOTf, respectively, whereas it was hardly attenuated in the case of KOTf albeit with slight loss under the influence of its narrower stability window. When the current density was finally lowered from 125 to 1 mA cm^{-2} at the 61st cycle and thereafter, all half-cells recovered the capacity nearly equal or slightly inferior to their initial value. These results may indicate that there was virtually no deterioration of $[Zn(dmpz)_2NDI]_n$-MOF electrode after repeated cycles at a wide range of current density. The excellent rate performance observed with the KOTf electrolyte especially at higher current density was largely caused by its better ionic conductivity and lower viscosity discussed in Fig. 4a, b, and d. Furthermore, we believe that the smaller hydrated K^+ ion could travel at higher speed even within the pore of $[Zn(dmpz)_2NDI]_n$-MOF electrode, in marked contrast to the larger Li^+ and Na^+ ions at lower speeds, though the detailed study on the ion diffusivity such as EIS and GITT in the near future may reinforce these qualitative discussions.

Unlike the half-cell of $[Zn(dmpz)_2NDI]_n$-MOF electrode (Fig. 5c), the half-cell of $A_2Ni[Fe(CN)_6]$ PBA electrode in 8 m AOTf aqueous electrolytes (A = Na, K) showed only little difference in the rate performance even at higher current density above 100 mA cm^{-2} as shown in Fig. 5a. These results may suggest that the pore size provided by the PBA electrode was not large enough for hydrated Na^+ and K^+ ions. Therefore, both could go into the pore only after dehydration and the difference in the total travel time became negligible. Furthermore, the full-cell combining these two electrodes no longer showed kinetic difference between Na^+ and K^+-based aqueous

Table 3 Parameters of alkaline metal triflate aqueous electrolytes

	LiOTf aq		NaOTf aq		KOTf aq	
Concentration	1 m	8 m	1 m	8 m	1 m	8 m
Conductivity/mS cm^{-1}	42	59	52	88	68	133
Density/g cm^{-3}	1.07	1.40	1.09	1.45	1.09	1.47
Viscosity/mPa s	1.14	5.91	1.07	5.33	0.98	3.77

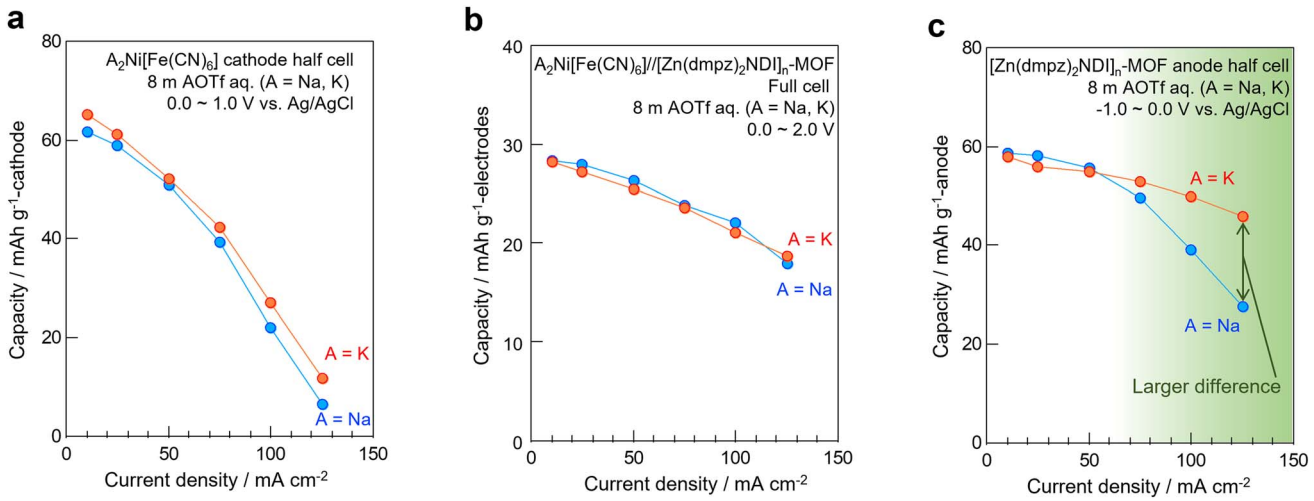

Fig. 5 Rate capability of (a) $A_2Ni[Fe(CN)_6]$, (c) $[Zn(dmpz)_2NDI]_n$-MOF, and (b) their full-cell in 8 m AOTf aq (A = Na, K), respectively. These were rebuilt based on the raw data shown in Fig. S3.†

electrolytes at a broad range of current density as shown in Fig. 5b. Therefore, we may conclude that K^+-based aqueous electrolyte is fundamentally beneficial in terms of rate performance, but we can only appreciate the merit when we employ appropriate electrode materials that have sufficiently large pores to accommodate its hydrated ion without difficulty. To emphasize this conclusion, we separately illustrated the Ragone plot for the full-cells separately in Fig S3.† However, we have to be careful not to confuse the kinetic information with the potential difference of cathodes.

Experimental section/methods

Preparation of electrode materials

$H_2(dmpz)_2NDI$ and $[Zn(dmpz)_2NDI]_n$-MOF were prepared according to the reported procedure[20] as shown in Scheme S1.† $H_2(dmpz)_2NDI$ was characterized by JEOL JNM-ECA 600 spectrometer (^1H NMR at 600 MHz, $^{13}C\{^1H\}$ NMR at 150 MHz) using $(CD_3)_2SO$, to check its identity and purity by comparison with the reported spectra. $[Zn(dmpz)_2NDI]_n$-MOF was characterized by powder X-ray diffraction (XRD) using Rigaku Miniflex 600 X-ray diffractometer using Cu-Kα radiation, to confirm its crystal structure[20] (Fig. S1a†). To determine the remaining content of DMF in thus obtained $[Zn(dmpz)_2NDI]_n$-MOF, thermogravimetric analysis (TGA) was performed on a Rigaku Thermo Plus TG8110 under a nitrogen gas flow (Fig. S1b†). The local structures depicted in Fig. 1a as well as Fig. S2† were graphically rebuilt based on the reported data. $Na_2Ni[Fe(CN)_6]$ and $K_2Ni[Fe(CN)_6]$ were prepared by co-precipitation methods according to the reported methods.[55,56] The chemical compositions of $Na_2Ni[Fe(CN)_6]$ and $K_2Ni[Fe(CN)_6]$ were estimated by EDS (JEOL JCM-7000) as $Na_{1.0}Ni[Fe(CN)_6]_{0.8}\cdot 2.8H_2O$ (theoretical capacity is approximately 75 mA h g^{-1}) and $K_{1.5}Ni[Fe(CN)_6]_{0.9}\cdot 1.8H_2O$ (theoretical capacity is approximately 71 mA h g^{-1}), respectively.

Preparation of aqueous electrolytes

Aqueous electrolytes were prepared by dissolving the appropriate amounts of $NaClO_4$ (98%; Kishida), LiOTf (98.0%; TCI), NaOTf (98.0%; TCI), or KOTf (98.0%; TCI) in ultra-pure water (Merck KGaA, Direct-Q UV 3). These electrolytes were characterized by ATR-FT-IR (Thermo Fisher Scientific, Nicolet iS5), conductivity meter (Mettler Toledo, SevenExcellence S479), pH meter (HORIBA, LAQUAact D73-T), viscosity meter (A&D, SV-1A), and density meter (Anton Paar, DMA 35).

Electrochemical measurements

To improve the electronic conductivity, acetylene black (AB, DENKA) was mixed with electrode materials at a weight ratio of 25 : 70. The composites were mixed with polytetrafluoroethylene binder (PTFE) (Polyflon F-104; Daikin Industries) at a weight ratio of 95 : 5 to prepare the electrode pellets. They were shaped into disc of 3 mm diameter, which were sandwiched between sheets of titanium mesh (Thank-Metal) for electrochemical measurements. Three-electrode electrochemical beaker-type half cells with aqueous electrolytes were used in cyclic voltammetry (CV) and galvanostatic charge/discharge tests. Ag/AgCl electrode with saturated KCl (BAS Inc., RE-1CP) and activated carbon (AC) electrode were used as the reference and counter electrodes, respectively. For coin-type full cell, the cathode/anode weight balance was adjusted to 1/1 to fix cathode/anode capacity balance as approximately 1/1 (Fig. S4†). Linear sweep voltammetry (LSV) and CV were performed at a scan rate of 0.5 mV s^{-1} (AMETEK, VersaSTAT 3), and galvanostatic charge/discharge tests were carried out using a cycler (NAGANO & Co.) at constant current density.

Ex situ IR, XPS and XRD

Ex situ IR (JASCO, FT-IR 680 plus), X-ray photoelectron spectroscopy (XPS) (JEOL, JPS-9010 MC/IV; Mg-Kα) and *ex situ* XRD were carried out to study the electrochemical change of $[Zn(dmpz)_2NDI]_n$-MOF after the first discharge and the first charge in 17 m $NaClO_4$ aqueous electrolyte as follows; The used cell was disassembled in an Ar-filled glove box and the retrieved anode material was immersed in distilled water for 30 min and then vacuum dried for 3 h to prepare samples, which were transferred under Ar atmosphere to the IR, XPS and XRD instruments.

Conclusion

A new strategy to exploit maximum rate performance in aqueous battery was demonstrated by use of $[Zn(dmpz)_2NDI]_n$-MOF electrode, which showed excellent electrochemical properties in aqueous electrolytes. This study showed that a rational design of electrode material that allows hydrated ions travel freely even in its pore may contribute significantly to the improvement of rate performance. Such electrode materials with sufficiently large pores allow hydrated charge carriers to undergo co-insertion directly from the electrolyte. Along this line, exploration of suitable cathode materials is now underway to complete the configuration of high-rate aqueous K^+-ion battery.

Conflicts of interest

The authors declare no conflict of interest.

Acknowledgements

This work was financially supported by Grant-in-Aid for Scientific Research program (Grant Number JP19K15679 and JP23K04910), supported in part by the Elements Strategy Initiative for Catalysts and Batteries (ESICB) project (Grant Number JPMXP0112101003), Ministry of Education, Culture, Sports, Science and Technology of Japan (MEXT), and supported in part by "Dynamic Alliance for Open Innovation Bridging Human, Environment and Materials" from the MEXT.

References

1 H. Kim, J. Hong, K.-Y. Park, H. Kim, S.-W. Kim and K. Kang, *Chem. Rev.*, 2014, **114**, 11788–11827.

2 N. Alias and A. A. Mohamad, *J. Power Sources*, 2015, **274**, 237–251.
3 J. Liu, C. Xu, Z. Chen, S. Ni and Z. X. Shen, *Green Energy Environ.*, 2018, **3**, 20–41.
4 D. Chao, W. Zhou, F. Xie, C. Ye, H. Li, M. Jaroniec and S.-Z. Qiao, *Sci. Adv.*, 2020, **6**, eaba4098.
5 S. Muench, A. Wild, C. Friebe, B. Häupler, T. Janoschka and U. S. Schubert, *Chem. Rev.*, 2016, **116**, 9438–9484.
6 Q. Zhao, Y. Lu and J. Chen, *Adv. Energy Mater.*, 2017, **7**, 1601792.
7 X. Yin, S. Sarkar, S. Shi, Q.-A. Huang, H. Zhao, L. Yan, Y. Zhao and J. Zhang, *Adv. Funct. Mater.*, 2020, **30**, 1908445.
8 Y. Lu and J. Chen, *Nat. Rev. Chem.*, 2020, **4**, 127–142.
9 W. Zhang, W. Huang and Q. Zhang, *Chem.–Eur. J.*, 2021, **27**, 6131–6144.
10 K. Holguin, M. Mohammadiroudbari, K. Qin and C. Luo, *J. Mater. Chem. A*, 2021, **9**, 19083–19115.
11 D. J. Kim, Y. H. Jung, K. K. Bharathi, S. H. Je, D. K. Kim, A. Coskun and J. W. Choi, *Adv. Energy Mater.*, 2014, **4**, 1400133.
12 A. E. Lakraychi, K. Fahsi, L. Aymard, P. Poizot, F. Dolhem and J. P. Bonnet, *Electrochem. Commun.*, 2017, **76**, 47–50.
13 Y. Shi, H. Tang, S. Jiang, L. V. Kayser, M. Li, F. Liu, F. Ji, D. J. Lipomi, S. P. Ong and Z. Chen, *Chem. Mater.*, 2018, **30**, 3508–3517.
14 M. Na, Y. Oh and H. R. Byon, *Chem. Mater.*, 2020, **32**, 6990–6997.
15 H. Qin, Z. P. Song, H. Zhan and Y. H. Zhou, *J. Power Sources*, 2014, **249**, 367–372.
16 S. Qiu, Y. Xu, X. Li, S. K. Sandstrom, X. Wu and X. Ji, *Electrochem. Commun.*, 2021, **122**, 106880.
17 S. Jhulki, C. H. Feriante, R. Mysyk, A. M. Evans, A. Magasinski, A. S. Raman, K. Turcheniuk, S. Barlow, W. R. Dichtel, G. Yushin and S. R. Marder, *ACS Appl. Energy Mater.*, 2020, **4**, 350–356.
18 Y. Zhou and L. Han, *Coord. Chem. Rev.*, 2021, **430**, 213665.
19 L. Kong, M. Cheng, H. Huang, J. Pang, S. Liu, Y. Xu and X. Bu, *EnergyChem*, 2022, **4**, 100090.
20 C. R. Wade, T. Corrales-Sanchez, T. C. Narayan and M. Dincă, *Energy Environ. Sci.*, 2013, **6**, 2172–2177.
21 C. R. Wade, M. Li and M. Dincă, *Angew. Chem. Int., Ed.*, 2013, **52**, 13377–13381.
22 N. Masciocchi, S. Galli and A. Sironi, *Comments Inorg. Chem.*, 2005, **26**, 1–37.
23 C. Wang, X. Liu, N. Keser Demir, J. P. Chen and K. Li, *Chem. Soc. Rev.*, 2016, **45**, 5107–5134.
24 V. Colombo, S. Galli, H. J. Choi, G. D. Han, A. Maspero, G. Palmisano, N. Masciocchi and J. R. Long, *Chem. Sci.*, 2011, **2**, 1311–1319.
25 H. J. Choi, M. Dincă, A. Dailly and J. R. Long, *Energy Environ. Sci.*, 2010, **3**, 117–123.
26 M. J. Kalmutzki, C. S. Diercks and O. M. Yaghi, *Adv. Mater.*, 2018, **30**, 1704304.
27 K. Nakamoto, R. Sakamoto, M. Ito, A. Kitajou and S. Okada, *Electrochemistry*, 2017, **85**, 179–185.
28 K. Nakamoto, R. Sakamoto, Y. Sawada, M. Ito and S. Okada, *Small Methods*, 2019, **3**, 1800220.
29 S. Dhir, S. Wheeler, I. Capone and M. Pasta, *Chem*, 2020, **6**, 2442–2460.
30 X. Zhang, T. Xiong, B. He, S. Feng, X. Wang, L. Wei and L. Mai, *Energy Environ. Sci.*, 2022, **15**, 3750–3774.
31 T. Hosaka, A. Noda, K. Kubota, K. Chiguchi, Y. Matsuda, K. Ida, S. Yasuno and S. Komaba, *ACS Appl. Mater. Interfaces*, 2022, **14**, 23507–23517.
32 D. Su, A. McDonagh, S. Qiao and G. Wang, *Adv. Mater.*, 2017, **29**, 1604007.
33 L. Jiang, Y. Lu, C. Zhao, L. Liu, J. Zhang, Q. Zhang, X. Shen, J. Zhao, X. Yu, H. Li, X. Huang, L. Chen and Y. S. Hu, *Nat. Energy*, 2019, **4**, 495–503.
34 K. Miyazaki, N. Takenaka, E. Watanabe, Y. Yamada, Y. Tateyama and A. Yamada, *ACS Appl. Mater. Interfaces*, 2020, **12**, 42734–42738.
35 S. Ko, Y. Yamada and A. Yamada, *Electrochem. Commun.*, 2020, **116**, 106764.
36 Q. Zheng, S. Miura, K. Miyazaki, S. Ko, E. Watanabe, M. Okoshi, C. Chou, Y. Nishimura, H. Nakai, T. Kamiya, T. Honda, J. Akikusa, Y. Yamada and A. Yamada, *Angew. Chem. Int., Ed.*, 2019, **58**, 14202–14207.
37 C. D. Wessells, S. V. Peddada, R. A. Huggins and Y. Cui, *Nano Lett.*, 2011, **11**, 5421–5425.
38 K. Hurlbutt, S. Wheeler, I. Capone and M. Pasta, *Joule*, 2018, **2**, 1950–1960.
39 B. Wang, Y. Han, X. Wang, N. Bahlawane, H. Pan, M. Yan and Y. Jiang, *iScience*, 2018, **3**, 110–133.
40 S. Qiu, Y. Xu, X. Wu and X. Ji, *Electrochem. Energy Rev.*, 2022, **5**, 242–262.
41 M. Ishizaki, H. Ando, N. Yamada, K. Tsumoto, K. Ono, H. Sutoh, T. Nakamura, Y. Nakao and M. Kurihara, *J. Mater. Chem. A*, 2019, **7**, 4777–4787.
42 M. Asai, A. Takahashi, K. Tajima, H. Tanaka, M. Ishizaki, M. Kurihara and T. Kawamoto, *RSC Adv.*, 2018, **8**, 37356–37364.
43 S. Yagi, M. Fukuda, T. Ichitsubo, K. Nitta, M. Mizumaki and E. Matsubara, *J. Electrochem. Soc.*, 2015, **162**, A2356–A2361.
44 S. Phadke, R. Mysyk and M. Anouti, *J. Energy Chem.*, 2020, **40**, 31.
45 S. Saeed, S. Boyd, W.-Y. Tsai, R. Wang, N. Balke and V. Augustyn, *Chem. Commun.*, 2021, **57**, 6744–6747.
46 R. Sakamoto, M. Yamashita, K. Nakamoto, Y. Zhou, N. Yoshimoto, K. Fujii, T. Yamaguchi, A. Kitajou and S. Okada, *Phys. Chem. Chem. Phys.*, 2020, **22**, 26452–26458.
47 K. Nakamoto, R. Sakamoto, Y. Nishimura, J. Xia, M. Ito and S. Okada, *Electrochemistry*, 2021, **89**, 415–419.
48 M. H. Lee, S. J. Kim, D. Chang, J. Kim, S. Moon, K. Oh, K.-Y. Park, W. M. Seong, H. Park, G. Kwon, B. Lee and K. Kang, *Mater. Today*, 2019, **29**, 26–36.
49 Z. Meng, C. G. Jones, S. Farid, I. U. Khan, H. M. Nelson and K. A. Mirica, *Angew. Chem. Int., Ed.*, 2021, **61**, e202113569.
50 Y. Yamada, K. Usui, K. Sodeyama, S. Ko, Y. Tateyama and A. Yamada, *Nat. Energy*, 2016, **1**, 16129.
51 L. Suo, O. Borodin, T. Gao, M. Olguin, J. Ho, X. Fan, C. Luo, C. Wang and K. Xu, *Science*, 2015, **350**, 938–943.
52 L. Suo, O. Borodin, W. Sun, X. Fan, C. Yang, F. Wang, T. Gao, Z. Ma, M. Schroeder, A. von Cresce, S. M. Russell,

M. Armand, A. Angell, K. Xu and C. Wang, *Angew. Chem. Int., Ed.*, 2016, **55**, 7136–7141.

53 L. Suo, O. Borodin, Y. Wang, X. Rong, W. Sun, X. Fan, S. Xu, M. A. Schroeder, A. V. Cresce, F. Wang, C. Yang, Y.-S. Hu, K. Xu and C. Wang, *Adv. Energy Mater.*, 2017, **7**, 1701189.

54 W. Xu, E. I. Cooper and C. A. Angell, *J. Phys. Chem. B*, 2003, **107**, 6170–6178.

55 X. Wu, C. Wu, C. Wei, L. Hu, J. Qian, Y. Cao, X. Ai, J. Wang and H. Yang, *ACS Appl. Mater. Interfaces*, 2016, **8**, 5393–5399.

56 J. Peng, J. Wang, H. Yi, W. Hu, Y. Yu, J. Yin, Y. Shen, Y. Liu, J. Luo, Y. Xu, P. Wei, Y. Li, Y. Jin, Y. Ding, L. Miao, J. Jiang, J. Han and Y. Huang, *Adv. Energy Mater.*, 2018, **8**, 1702856.